

PCCP

Accepted Manuscript



This is an *Accepted Manuscript*, which has been through the Royal Society of Chemistry peer review process and has been accepted for publication.

Accepted Manuscripts are published online shortly after acceptance, before technical editing, formatting and proof reading. Using this free service, authors can make their results available to the community, in citable form, before we publish the edited article. We will replace this *Accepted Manuscript* with the edited and formatted *Advance Article* as soon as it is available.

You can find more information about *Accepted Manuscripts* in the [Information for Authors](#).

Please note that technical editing may introduce minor changes to the text and/or graphics, which may alter content. The journal's standard [Terms & Conditions](#) and the [Ethical guidelines](#) still apply. In no event shall the Royal Society of Chemistry be held responsible for any errors or omissions in this *Accepted Manuscript* or any consequences arising from the use of any information it contains.

Cite this: DOI: 10.1039/c0xx00000x

www.rsc.org/xxxxxx

ARTICLE TYPE

MesoScale Simulation of the Formation and Dynamics of Lipid-structured Poly(ethylene oxide)-*block*-Poly(methyl methacrylate) Diblock Copolymers

Dan Mu^{*a,b}, Jian-Quan Li^b, Sheng-Yu Feng^{*c} and Yi-Ping Cui^{*a}

5 Received (in XXX, XXX) Xth XXXXXXXXX 20XX, Accepted Xth XXXXXXXXX 20XX
DOI: 10.1039/b000000x

Twelve poly(ethylene oxide)-*block*-poly(methyl methacrylate) (PEO-*b*-PMMA) copolymers with lipid-like structures were designed and investigated by MesoDyn simulation. Spherical and worm-like micelles as well as bicontinuous, lamellar and defected lamellar phases were obtained. A special structure, designated as B2412, with two lipid structures connected by their heads, was found to undergo four stages prior to forming a spherical micelle phase. Two possible assembly mechanisms were found via thermodynamic and dynamic process analyses; namely, the fusion and fission of micelles in dynamic equilibrium during the adjustment stage. Water can be encapsulated into these micelles, which can affect their size, particularly in low concentration aqueous solutions. The assignment of weak negative charges to the hydrophilic EO blocks resulted in a clear effect on micelle size. Surprisingly, the largest effect was observed with EO blocks with -0.5 e, wherein an ordered perfect hexagonal phase was formed. The obtained results can be applied in numerous fields of study, including adsorption, catalysis, controlled release and drug delivery.

1 Introduction

20 The self-assembly of block copolymers (BCP) has received increasing attention due to its potential application in a number of fields, including microelectronics, drug delivery devices and membranes. BCPs with ordered structures of spheres, cylinders or lamellae and controlled size would be useful in the manufacturing industry [1-3].

Poly(ethylene oxide) (PEO) has been widely utilized due to its biocompatibility, low toxicity and solubility in aqueous and organic solvents [4]. Amphiphilic BCPs with PEO and poly(methyl methacrylate) (PMMA) blocks are utilized in a range of applications, including keratoprostheses [5], drug carriers [6] and biomedical materials [7-9]. As reported in our previous work [10], we elucidated the lower critical solution temperature (LCST) behavior of PEO/PMMA blends at high temperatures and validated its miscibility behavior. Molecular modeling is useful in clarifying the conflicting conclusions drawn from different techniques and/or laboratories [11-13].

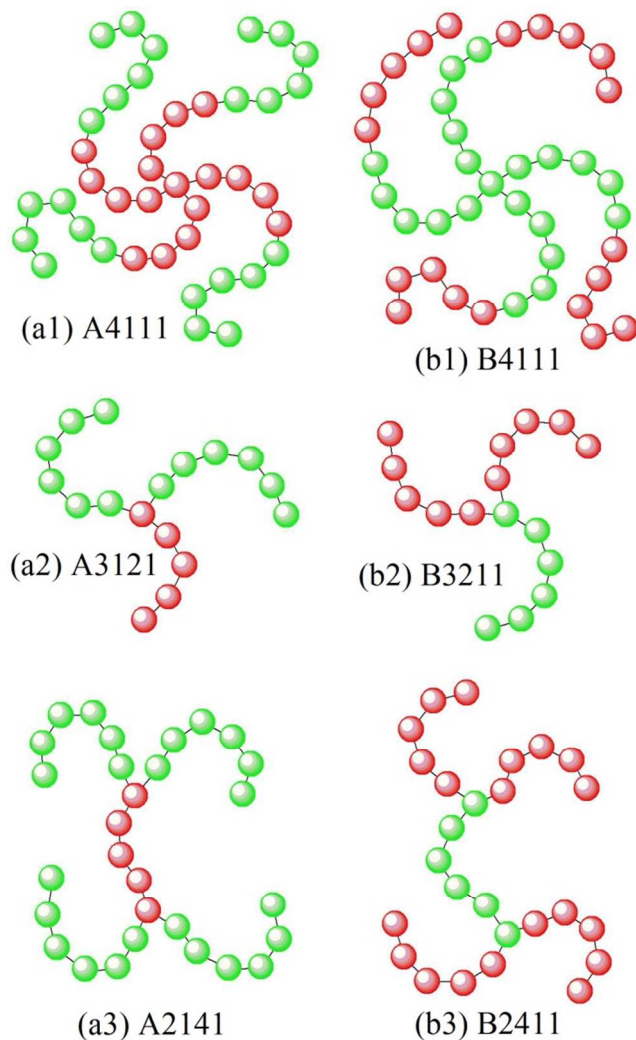
Although there are many experimental reports on polymer science, the rapid pace of polymerization hinders facile capturing of a material's changing details, which is significant in understanding its mechanics. For example, mesoscale structures are formed in a few milliseconds, and it is therefore difficult to comprehensively determine their growth mechanism experimentally. Fortunately, mesoscopic dynamic models form a bridge between the fast molecular kinetics and slow thermodynamic relaxation of macroscale properties and provide a

powerful tool to study phases and the kinetics of phase formation. The MesoDyn method is based on dynamic mean-field density functional theory (DDFT), developed by Fraaije [14-15], and the phase-separation dynamics and ordering processes of multicomponent polymeric systems are described by the Langevin equations. One of the most important advantages of this method is that there are no priori assumptions on the phases or on the kinetics of phase formation [16]. Many successful applications of the MesoDyn method have been previously demonstrated with phase separation [17-18], phase transition [19], and mesoscale structure formation in response to nanoparticle doping [20-21] or induced by surfaces [22-23]. Tong et al. synthesized well-defined PMMA-*b*-PEO-*b*-PMMA triblock copolymers with various PMMA and/or PEO block lengths, and observed micelle formation in aqueous solutions using steady fluorescence spectra with a pyrene probe, dynamic light scattering (DLS) and atomic force microscope (AFM) [24]. Varade group examined the formation and structural features of low molecular weight PEO-*b*-PMMA diblock copolymers in water, aqueous NaCl and aqueous urea solutions by using surface tension, dye spectra, cloud point, viscosity and small angle neutron scattering (SANS) measurements [25]. These experiments demonstrate that PEO-*b*-PMMA copolymers can only present mesoscale structures, such as micelles, when assisted by the solvent effect in a solution state. This phenomenon is due to the similar solubility parameters of PEO and PMMA, which results in the Flory-Huggins segmental interaction parameters (χ) in the full range of the composition to become nearly equal to each other. Different from the interaction between groups

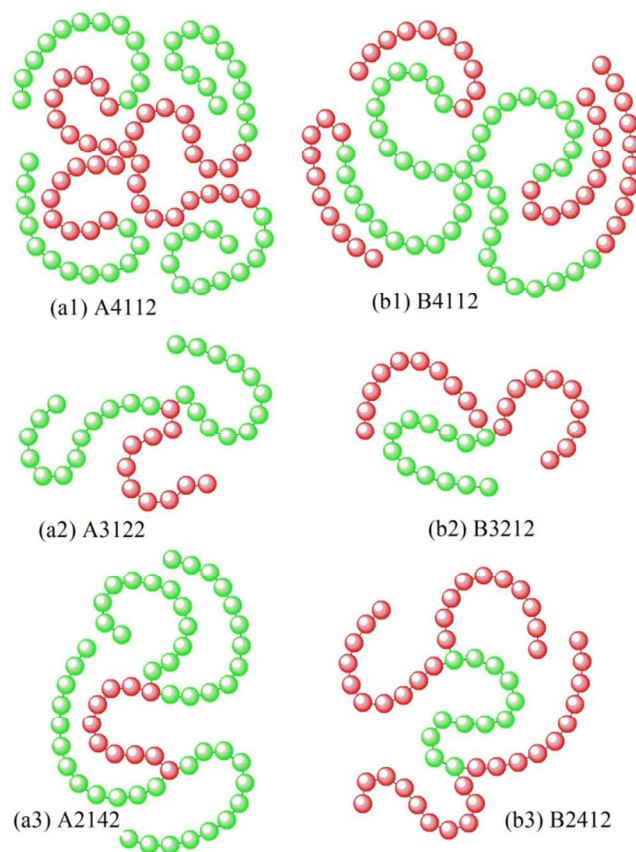
calculated on the atomic level [26-27], the description of χ can be a bridge between the microscale and the mesoscale, and the definition of χ is,

$$\chi = \left(\frac{\Delta E_{mix}}{RT} \right) V_{mon}$$

5 where V_{mon} is a monomer unit volume. In addition, the ΔE_{mix} is defined as $\Delta E_{mix} = \phi_1 \left(\frac{E_{coh}}{V} \right)_{pure} + \phi_2 \left(\frac{E_{coh}}{V} \right)_{mix} - \left(\frac{E_{coh}}{V} \right)_{mix}$, where ϕ is the volume fraction and the indices "pure" and "mix" denote the cohesive energy densities in parentheses, refer to the pure components and the binary mixture, respectively. The absolute values of χ calculated in our previous work were below 2×10^{-3} [10]. These values are quite small, which indicates that micelle formation is prevented in this block copolymer system.



15 **Fig. 1.** Schematic representation of miktoarm PEO-*b*-PMMA BCP models with short chains. The red particles represent the EO blocks denoted as A, and the green particles represent the MMA blocks denoted as B. (a1)-(a3) presents the molecular architecture of A4111, A3121 and A2141, respectively; (b1)-(b3) presents the molecular architecture of B4111, B3211 and B2411, respectively.



25 **Fig. 2.** Schematic representation of miktoarm PEO-*b*-PMMA BCP models with long chains. The red particles represent the EO blocks denoted as A, and the green particles represent the MMA blocks denoted as B. (a1)-(a3) presents the molecular architecture of A4112, A3122 and A2142, respectively; (b1)-(b3) presents the molecular architecture of B4112, B3212 and B2412, respectively.

The polymer properties mainly depend on the chemical composition and topology of the constituents. Therefore, the design of complex macromolecular architectures to control the polymer properties is a significant field in polymer science [28]. According to the chemical composition of the arm species, the star polymers can be classified into two categories, i.e., homoarm star polymer or heteroarm star polymer. The heteroarm star polymers have attracted much attention recently due to their distinctive morphological structures, bulk properties, solution properties, and their potential utility in nanoscience applications [29-31]. The morphologies and structures of the heteroarm star polymers in the bulk and solution states can be characterized by a variety of techniques [29-35], and they have potential applications in microelectronic, optical and optoelectronic devices. Lipid molecules can form abundant morphologies, such as lamellar phases or vesicles, which are useful in a number of important biological processes [36]. In the present work, we mimic the molecular topology of lipid molecules in our design of six heteroarm (miktoarm) PEO-*b*-PMMA BCPs with the aims of determining the ordered morphologies formed by these PEO-*b*-PMMA BCPs and thoroughly investigating phase transformation during the self-assembly processes with the MesoDyn method. Some effects of adjusting the aggregation size are discussed to illuminate the relationship between influencing factors and resulting aggregate sizes.

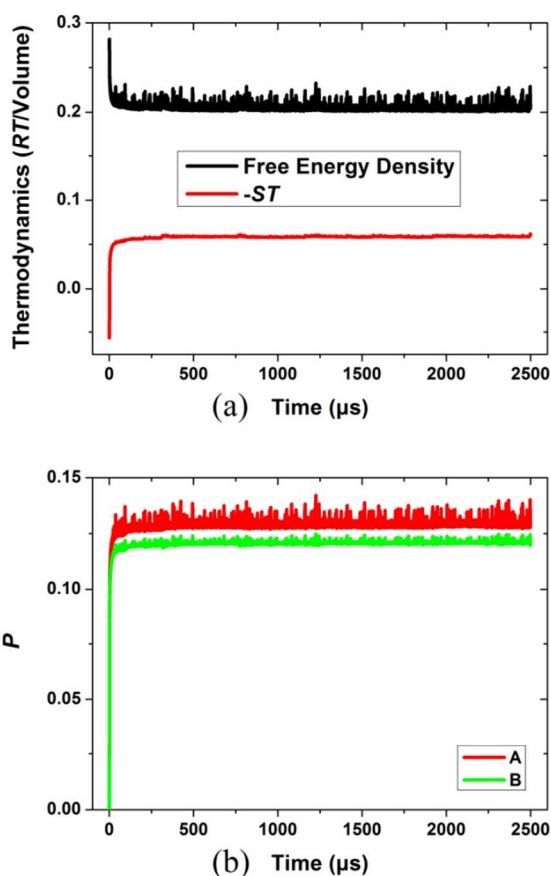


Fig. 3. The evolution of (a) the free energy density, $-ST$ and (b) P values with time for B2412 copolymer.

2 Models and Parameter Settings

The MesoDyn method uses a coarse-grained definition of molecules with a Gaussian chain description. Segments are defined as several beads of the same size, and the detailed atomic information on the chain topology depends upon the degree of coarsening of the original chain. Therefore, two sets of parameters should be specified in MesoDyn simulations: the molecular topology described by beads and the interaction energies of the various bead types.

First, we built ten of statistical PEO and PMMA homopolymer chains with various chain lengths, respectively. After calculated their cohesive energy density via molecular dynamic simulation methods and compared with their experimental data within a reasonable tolerance, the representative chain lengths of PEO and PMMA were obtained as PEO₅₀ and PMMA₅₀, which are both the shortest chain lengths can be used to study their bulk properties.

The coarse-grained length of atomic PEO₅₀ and PMMA₅₀ are decided by the division of the atomic length by the characteristic ratio (C_∞), i.e., for PEO, the coarse-grained length of PEO₅₀ should be 50 divided by 9.89 equals to 5 approximately; for PMMA, it should be 50 divided by 8.65 equals to 6 approximately. Therefore, A₅ and B₆ (A and B represent PEO and PMMA segments, respectively) can be applied to represent the atomistic chains of the polymers PEO₅₀ and PMMA₅₀, and it's also they are also the mesoscale models of homopolymers. In our simulations, we set A₅B₆ as a basic unit for investigation, and

designed six types of chain topologies for PEO-*b*-PMMA BCPs, as illustrated in Fig. 1. To investigate the phase morphologies of different chain lengths, we enlarged one time in chain lengths of the structures in Fig. 1 to produce another six BCPs, which are listed in Fig. 2. To name these BCPs, the letter denotes the bead type of the branched point, the first number is equal to the arm number for each branched point, the following two numbers represent A to B segment ratio, and the last number describes the chain length according to the multiples of the A₅ and B₆ segments. Taking B2412 as an example, this BCP consists of two branched points made of B bead, each branched point has two arms, the A to B segment ratio is 4:1, each of the A and B segments are two times the chain length of the A₅ and B₆ segment. The molecular information of all twelve BCPs is listed in Table 1.

Table 1 Molecular information of the BCPs.

Name	Arm number in each branch point	Ratio of A to B segments	Chain length*	Molecular structure
A4111	4	1:1	1	A(A ₄ B ₆) ₄
A3121	3	1:2	1	A ₄ A(B ₆) ₂
A2141	2	1:4	1	(B ₆) ₂ AA ₃ A(B ₆) ₂
B4111	4	1:1	1	B(B ₅ A ₅) ₄
B3211	3	2:1	1	B ₃ B(A ₅) ₂
B2411	2	4:1	1	(A ₅) ₂ BB ₄ B(A ₅) ₂
A4112	4	1:1	2	A(A ₉ B ₁₂) ₄
A3122	3	1:2	2	A ₉ A(B ₁₂) ₂
A2142	2	1:4	2	(B ₁₂) ₂ AA ₈ A(B ₁₂) ₂
B4112	4	1:1	2	B(B ₁₁ A ₁₀) ₄
B3212	3	2:1	2	B ₁₁ B(A ₁₀) ₂
B2412	2	4:1	2	(A ₁₀) ₂ BB ₁₀ B(A ₁₀) ₂

* Describes the multiple of chain length based on A₅ and B₆.

The interaction energies, ϵ_{AB} , between various types of beads are defined as the χ value among different segments multiplied by RT , where R is the molar gas constant, and T is 400 K. A positive ϵ_{AB} parameter indicates a repulsion interaction between A and B beads. The local gradients of chemical potentials provide the driving forces. Then, the dynamics of the component densities are described by a set of functional Langevin equations. The parameters were chosen based on our previous study [10] and then converted into the interaction energy value utilized in MesoDyn calculations. The ϵ_{AB} data of unlike-species are listed in Table 2, in addition, the interaction energy between the like-species is all 0, i.e., $\epsilon_{AA}=0$ and $\epsilon_{BB}=0$.

Table 2 ϵ_{AB} data converted from χ values via molecular dynamic simulations at 400 K.

Ratio of A to B segments	ϵ_{AB}
1:1	3.61
1:2	1.14
1:4	0.24
2:1	4.68
4:1	6.23

For all simulations, the dimensions of the simulation lattice were set to a $32 \times 32 \times 32$ nm³ grid. The simulation parameters were chosen as follows: the bond length was set to 1.1543 to ensure isotropy of all grid-restricted operators; as an approximation, all bead diffusion coefficients were taken as 1.0×10^{-7} cm² · s⁻¹ to

ensure a stable numerical algorithm; the time step was 50.0 ns; a constant noise-scaling parameter of 100 was chosen, the compressibility parameter was fixed at 10.0; and the total simulation time was 50,000 steps, i.e., 2.5 ms.

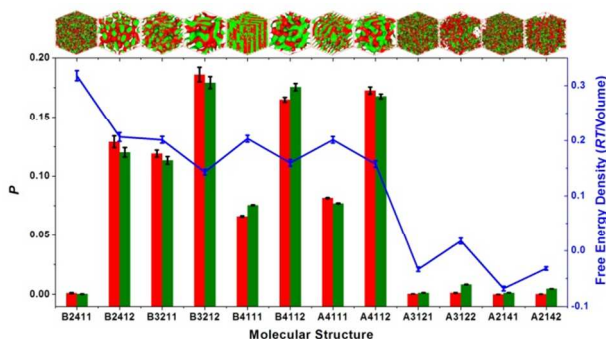


Fig. 4. P and free energy density values of PEO-*b*-PMMA BCPs. The red column contains the P value of EO blocks, and the green column contains the P value of the MMA blocks. The phase structures are listed on the top according to their order along the X axis. Red represents the A isosurface, whereas green represents the B isosurface.

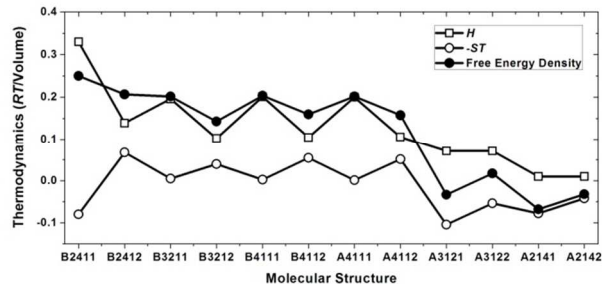


Fig. 5. Thermodynamic parameter values, H , $-ST$ and free energy density, of BCPs.

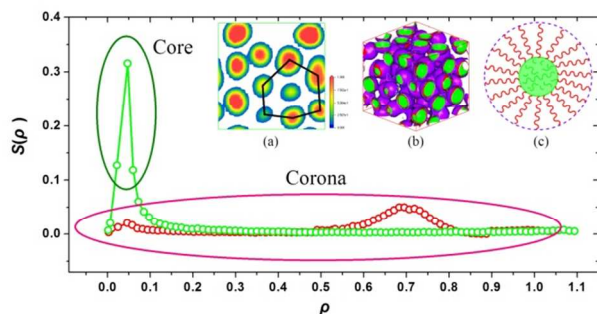


Fig. 6. Structure of the spheroidal micellar phase. (a) Density slice of MMA blocks. (b) Density field distributions of EO and MMA blocks in spheroidal micellar phase. (c) Schematic representation of spheroidal micellar phase.

3 Results and Discussion

The systems were set as homogenous dispersions at the beginning. With the evolution of the density fields of each bead, the free energy [37-38] should asymptotically approach a stable value as the system attains a dynamic equilibrium during the MesoDyn simulations, which serves as a good index of system stability. However, the free energy density is calculated based on the DDFT, which is not routinely calculated for real systems. Therefore,, it is not possible to make a direct comparison with

experimental free energy data [39].

The order parameter, P_i , is defined as the volume average of the 30 difference between the local density squared and the overall density squared, which reflects the effects of phase separation:

$$P_i = \frac{1}{V} \int [\eta_i^2(r) - \eta_i^2] dr,$$

where $\eta_i(r)$ is a dimensionless density (volume fraction) for species i of local density, and η_i is the overall density for species i . Hence, it is a significant index of the degree of phase separation, as a large value indicates strong phase segregation and a small value indicates a mixed state.

3.1 Aggregation structures of BCPs

Take B2412 copolymer as an example, Fig. 3 shows the evolution 40 of the free energy, the negative number of entropy times temperature ($-ST$) and the P values, they all approach to the certain values, which are the evidence of reaching the equilibrium state. The mesoscale structures are shown on the upper portion of Fig. 4. The observed phases are disordered, spherical micelles, 45 worm-like micelles, bicontinuous, lamellar, bicontinuous, defected lamellar, bicontinuous, disordered, disordered and disordered in sequence from left to right. Bicontinuous phases are formed when the chain is long and consists of similar or equal A to B segment ratios (B3212, B4112 and A4112), providing the highest P values. When the long chain has a higher arm number and an equal A to B segment ratio (B4111), BCPs can form a lamellar phase. However, when an A segment is exchanged in place of the B segment in B4111 (A4111), the ordered lamellar structure is perforated by several 55 holes and necks, and is therefore defected lamellar. B3211 has a lipid-like structure, with both hydrophobic and hydrophilic arms and short-chains, which produces worm-like micelles. When two hydrophilic arms are added at the end of the B segment, the molecular structure of B2412 resembles a combination of two 60 B3212 BCPs joined together at the end of the hydrophobic B beads. This structure presents as ordered spherical micelles. The other BCPs have A as the branch point and higher B segment percentages, present as disordered phases with the lowest calculated order parameters. It is interesting that B2411 doesn't 65 become a micelle phase, which is attributed to its short-chained structure compared with that of B2412. We find several small aggregates with sizes below the nanometer magnitude, which cannot be seen as ordered phases at the mesoscale and therefore have low P values. However, the highest free energy density 70 indicates that B2411 is in the pre-micelle phase and is not stable. Fig. 5 shows the thermodynamic properties of enthalpy (H), $-ST$ and free energy density. The relationships among H , $-ST$ and free energy density indicate that enthalpy has the largest influence on BCP phase morphologies. Owing to the two highest values of 75 B2411 and B2412 in the free energy density, combined with the disordered phase of B2411 and the spherical micelles phase of B2412, what we discuss followed is mainly on B2412 copolymer.

3.2 Analysis of phase morphology of B2412 BCP

Micellar phase morphology was typical in the studies of BCPs 80 above, particularly for B2412. A unimodal and narrow peak in the density field distributions in Fig. 6 reveals that the hydrophobic MMA blocks aggregate to form a very high-density core micelle structure, whereas the hydrophilic PEO constitute the corona structure. Some of the spheroidal micelles tend to

arrange hexagonally as shown in Fig. 6a. To gain a deeper insight into this structure, we highlighted the end of each hydrophilic EO block arm in purple, and ran the calculation again. The stable structure shown in Fig. 6b indicates that the outer of the corona is composed of the ends of the arms. The core-shell structure of the spheroidal micelle is shown in Fig. 6c.

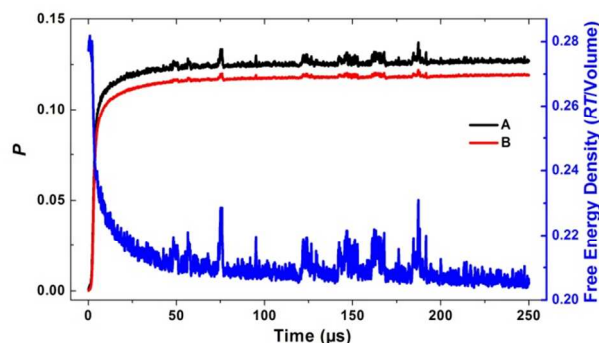


Fig. 7. Time evolution of P and free energy density during the mesophase formation of B2412 BCP.

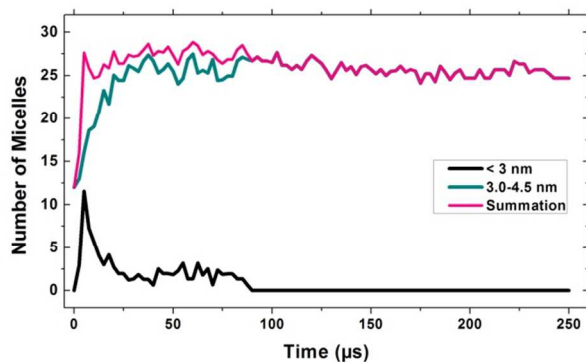


Fig. 8. Statistics on the number of micelles over time.

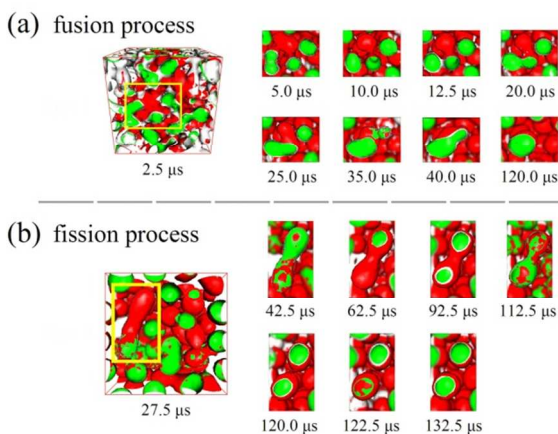


Fig. 9. Process of (a) fusion and (b) fission of spherical micelles over time. The area enclosed by the yellow box is enlarged and to the right to show the process details.

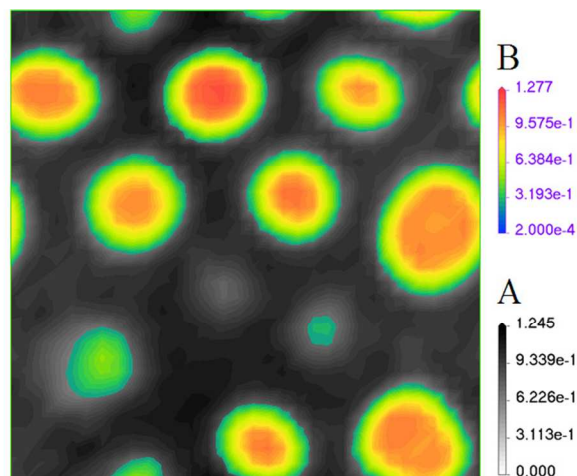


Fig. 10. Density slice of EO (with white-black legend) and MMA (with reverse rainbow legend) blocks.

3.3 Transition phase structure and mechanism of B2412 BCP

The dynamic evolution of the mesostructure can be confirmed by both the order parameter and free energy density over time. In Fig. 7, four stages of micellar evolution can be seen, referred to as the induction stage, reproduction stage, adjustment stage and equilibrium stage. In stage I, which lasts for less than $0.1 \mu\text{s}$, the morphology is homogeneous with low P values and high free energy density. In stage II, phase separation and subsequent the pre-micelle formation occurs over $5 \mu\text{s}$, resulting in increased P values and decreased free energy density. Then, the spherical micelles are formed from the pre-micelles. In stage III, the P values continue to increase and the free energy density continues to decrease, but the rates of change are much slower than those in stage II. Notably, both the order parameter and the free energy density switch to higher values several times. This phenomenon is a result of the abrupt or coalescent behavior of the micelles and lasts for approximately $190 \mu\text{s}$, during which the micelle number, shape and size adjusts. Finally, both the P and free energy density values stabilize, which indicates that the system has arrived at a thermodynamic and dynamic equilibrium state, i.e., stage IV.

To analyze the dynamic process, the amount of micelles versus simulation time is shown in Fig. 8. We found that the number of both small- and large-sized micelles is equivalent in stage II, where the sum of the two types of micelles is the highest. This micelle production is in preparation for the next stage. Early in stage III, the number of small-sized micelles decreases rapidly, whereas the number of large-sized micelles increases rapidly. These alterations indicate that the small-sized micelles fuse into larger micelles. Subsequently, the number of small-sized micelles increases by a small amount, whereas the number of large-sized micelles decreases slightly, indicating that the large-sized micelles split into smaller micelles at this point.

The mechanisms of fusion and fission are illustrated in Fig. 9. In fusion, there is a large, irregularly shaped parent aggregate with three connected micro-aggregates with narrow necks at $5.0 \mu\text{s}$. Both of the micro-aggregates on the sides are expelled from the parent aggregate after $5.0 \mu\text{s}$ and subsequently move close to the center micro-aggregate. They initially connect their shells together, and then their cores fuse together in a peanut shell shape

over 7.5 μs . Then, the narrow neck between the micro-aggregates and the parent aggregate becomes thicker, until they all join together. At the same time, the micro-aggregate on the right forms a bud on the parent aggregate and transfers its core, so that the two share shell and form a large aggregate over 5.0 μs . Over 80 μs , the large aggregate adjusts its shape from sub-elliptical to spherical. To analyze fission, a large peanut-shaped aggregation was chosen at a starting point of 42.5 μs . During the first 30.0 μs , all MMA blocks re-orient in the micelle, allowing the EO blocks to act as the shell. The uneven distribution of EO and MMA blocks is followed by narrowing of the middle portion of the aggregate. After 10.0 μs , the aggregate separates into two independent spherical micelles. It takes 10.0 μs to re-adjust the orientation of the EO and MMA blocks, upon which two perfect core-shell micelles are formed.

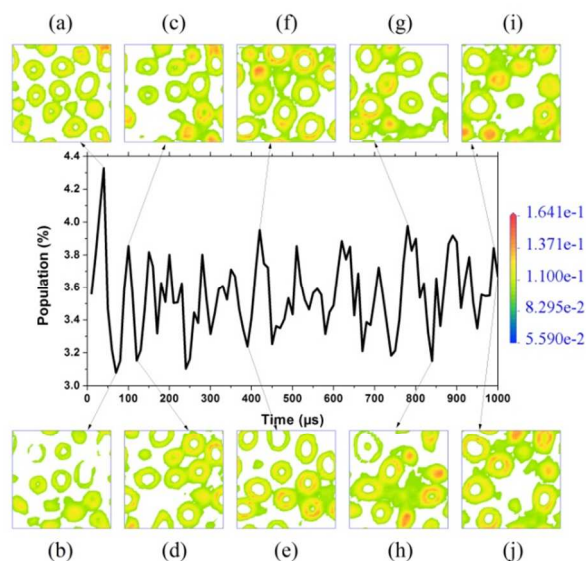


Fig. 11. Population of encapsulated water and the density slice of W beads over time. The concentration is 90 % (v/v). (a) 40 μs , (b) 70 μs , (c) 100 μs , (d) 120 μs , (e) 390 μs , (f) 420 μs , (g) 780 μs , (h) 840 μs , (i) 990 μs , (j) 1000 μs .

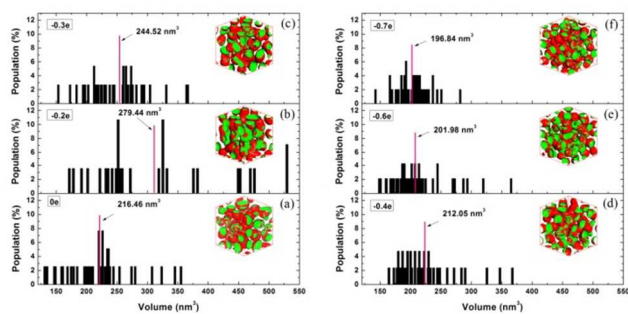


Fig. 12. Volume distribution of micelle aggregates for the A beads with (a) 0 e, (b) -0.2 e, (c) -0.3 e, (d) -0.4 e, (e) -0.6 e and (f) -0.7 e, in comparison with a neutral system. The magenta lines represent the average volumes for each system.

3.4 Function test of B2412 micelle phase

The density of MMA blocks radially decreases from the center of the micelle to the outer surface, whereas the EO block density increases in the same direction, as shown in Fig. 10. Thus, the

density between the core and corona is very low, with a small volume of empty space. This observation led us to wonder whether the micelle phase can be a vesicle carrier and the potential mechanism for this occurrence. To this end, we performed additional simulations in aqueous solution.

We estimated the Flory-Huggins parameter for water-polymer interaction as follows:

where δ_{water} and $\chi_{\text{polymer}} = \frac{(\delta_{\text{water}} - \delta_{\text{polymer}})^2}{RTV_s}$ are the Scatchard-Hildebrand solubility parameters of the solvent and the polymer, respectively [40], and V_s is the molar volume of the solvent molecules. Three water molecules are represented as one W bead. All other parameters were the same of those that were set for B2412 model.

The density slices and population of W in Fig. 11 illustrate the mechanism of micelle encapsulation of water. As only the EO blocks have good solubility in water the micelle size is uniform and quite small, with W beads encapsulated between the micelle core and corona, and the highest observed amount of encapsulated water. A synergistic effect is induced by high interfacial energy in the MMA-water interface and low interfacial energy in the EO-water interface that causes some micelles to break and induce water leakage and some to associate with other micelles. Due to the incompatibility of MMA blocks and water, the density evolution is driven by the shrinkage of MMA into small domains, which form smaller micelles. This occurrence proves the ability of micelles to enhance the solubility of insoluble, solvophobic molecules by trapping them in energetically compatible microenvironments [41-42]. The MMA blocks that aggregate into a larger core aim to expel water while forming a larger micelle. Therefore, the final micelles size is not uniform when solvent is involved.

Statistics on the average micelle size indicates that 10 % (v/v) water solvent addition causes a size increase of 6.21 %. However, size decreases of 4.28 %, 14.17 % and 16.72 % were observed in the cases with 15 % (v/v), 20 % (v/v) and 30 % (v/v) water solvent, respectively.

3.5 Charge effect of A beads on B2412 mesophase morphology

We performed ab initio calculations using Gaussian 03 software with the RM062X method and 6-311++G(d,p) basis set on PEO and PMMA homopolymers. The Mulliken charges per A and B beads were -0.21 and -0.03, respectively. Owing to the A beads act as the corona part in the core-shell structure, we assigned varied weak negative charges amounts to each A bead in series (-0.3 e, -0.4 e, -0.6 e and -0.7 e) via Donnan electrostatics treatment, and no charge was assigned to B beads due to their weak electrostatic interactions, aims to study the charge effect of A beads with different amount of charges on changing the B2412 phase morphologies. The salt strength is 0.01 mol·L⁻¹, to ensure the electro-neutrality of the whole system. These charged molecules were compared to the neutral B2412 system.

The images in Fig. 12 reveal that the final mesoscopic structures with -0.2 e (real charge of A beads), -0.3 e, -0.4 e, -0.6 e and -0.7 e charges assigned are all micelles. With the -0.2 e electrostatic effect, some aggregates deform into ellipsoid micellar clusters, to result in a broad size distribution, and the largest average micelle size. With increasing negative charges on the A beads, the coronas repel the cores, which obey the principle of repulsion

between similar electrostatic items. In addition, due to an even distribution of A beads around the core, the repulsive force from A beads is isotropic. This force condenses the B beads, so that the average size per micelle is reduced. The lowest polydispersity of A beads was observed with $-0.7 e$, which indicates that a series of uniformly-sized micelles formed. The average size per micelle increases by 29.10 % and 12.96 % when the A beads are assigned $-0.2 e$ and $-0.3 e$, respectively. Correspondingly, the size decreases by 2.04 %, 6.69 % and 9.06 % in the cases of A bead with $-0.4 e$, $-0.6 e$ and $-0.7 e$, respectively.

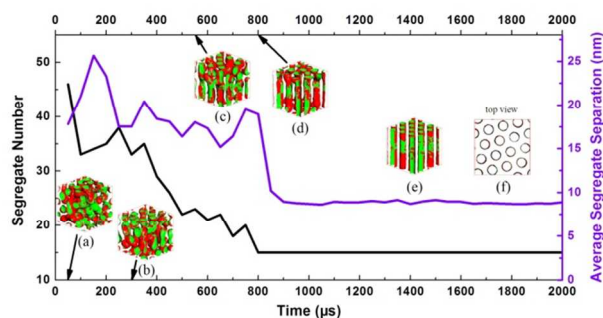


Fig. 13. Statistics on segregate number and average segregate separation over time. (a) 50 μs , (b) 300 μs , (c) 550 μs , (d) 800 μs . The last two phase morphologies are the final mesoscopic structures at 2000 μs in (e) side and (f) top view.

In the case of the A beads with $-0.5 e$ charge, as shown in Fig. 13, many spheroidal micelles form together initially with high number of segregates. The distance between segregates is short and with the $-0.5 e$ electrostatic interaction between A beads cause the cores to be pushed and squeezed. When this force loses balance and becomes anisotropic, the core and corona deform into “part-spherical-part-worm-like micelle” structures. With the coalescence of micelles, the associate structures are dragged and move in one direction, as demonstrated by the small fluctuation in the separation of segregates. When the main frame of columnar micelles is formed, an adjustment process of the tumid parts occurs in which they are reallocated in the direction along each column. Finally, a perfect-ordered hexagonal arrangement of columnar micelles with uniform size and shape is formed. The volume of each column is three times the size of each micelle.

4 Conclusions

The MesoDyn method was employed to investigate mesophase formation of PEO-*b*-PMMA copolymers. Ample phases of lipid structure-based PEO-*b*-PMMA BCPs were obtained which produced spherical, and worm-like micelles, as well as bicontinuous, lamellar and defected lamellar phases. Thus, the BCP structure is vital in forming mesoscale phases. Using analysis of P values, free energy density and changes in aggregate numbers, we found two mechanisms to explain the mesophase formation of the spherical micelle phase. Both the solvent choice and electrostatic interactions can alter micelle size. In particular, low solvent concentration (90 % v/v) and weak negative charges ($-0.2 e$ and $-0.3 e$) on A beads provide an increased micelle size, whereas the opposite conditions decrease micelle size. A special case with A beads with $-0.5 e$ charges was also evaluated. The mechanisms for uniform hexagonal phase

formation were successfully investigated to provide valuable information for adsorption, catalysis, controlled release, drug delivery and bio-mimetics.

Acknowledgments

This work is supported by the National Natural Science Foundation of China (21203164).

Supplement Information [43]

MesoDyn is based on a dynamic variant of mean-field density functional theory, and it states that there is a one-to-one mapping between the distribution functions of the system, the densities, and an external potential field. A real system with interactions can be equated to an ideal system via an effective external potential. The external potential can be found such that the distribution of the ideal system equals that of the real system at the same density. Therefore, this method is quite useful to describe the polymer fluids.

In MesoDyn, a real chain can be represented as a statistical Gaussian chain model via a factorization of the interactions. So the noninteracting Gaussian chains are the ideal system, and any interchain, i.e., non-bonded, interactions are treated as non-ideal. Furthermore, MesoDyn applies a further factorization of the external potential into an electrostatic and dispersive contribution. As a result, at an instant of time, a certain distribution of bead positions is described as a three-dimensional concentration fields, $\rho(r)$.

Dynamics

The derivation of the diffusive dynamics of the molecular ensemble is based on the assumption that for each type of bead, i , the local flux is proportional to the local bead concentration and the local thermodynamic driving force:

$$J_i = -M \rho_i \nabla \mu_i + J_i^{\square},$$

where J_i^{\square} is a stochastic flux (which can be thought of as a thermal noise). Combining this with the familiar continuity equation:

$$\frac{\partial \rho_i}{\partial t} + \nabla \cdot J_i = 0,$$

leads to simple diagonal functional Langevin equations (i.e., stochastic diffusion equations) in the component density fields:

$$\frac{\partial \rho_i}{\partial t} = M \nabla \cdot \rho_i \nabla \mu_i + \eta_i.$$

A Gaussian distribution of the noise is used.

However, the fluctuations in the total density of this simple system are not realistic since finite compressibility is not enforced by the mean-field potential chosen. Therefore, total density fluctuations are simply removed by introducing an incompressibility constraint:

$$(\rho_A(r, t) + \rho_B(r, t)) = 1/v_B,$$

where v_B is the average bead volume. This condition then leads to “exchange” Langevin equations:

$$\frac{\partial \rho_A}{\partial t} = M v_B \nabla \cdot \rho_A \rho_B \nabla [\mu_A - \mu_B] + \eta$$

and

$$\frac{\partial \rho_B}{\partial t} = M v_B \nabla \cdot \rho_A \rho_B \nabla [\mu_B - \mu_A] + \eta.$$

Here M is a bead mobility parameter, analogous to a self-diffusion coefficient. The kinetic coefficient $M v_B \rho_A \rho_B$ models a local exchange mechanism. So the model is strictly valid only for Rouse dynamics. Effects such as reptation lead to

kinetic coefficients which extend over a range of roughly the coil size. They lead to computationally expensive nonlocal operators which in addition, are very complex in the non-linear regime.

The distribution of the Gaussian noise satisfies the fluctuation-dissipation theorem:

$$\langle \eta(r, t) \rangle = 0 \text{ and}$$

$$\langle \eta(r, t) \eta(r', t') \rangle = -\frac{2Mv_B}{\beta} \delta(t-t') \nabla_r \cdot \delta(r-r') \rho_A \rho_B \nabla_{r'},$$

which ensures that the time integration of the Langevin equations generates an ensemble of density fields with Boltzmann distributions.

Thermodynamics

The dynamic Langevin equations contain the bead chemical potential as the thermodynamic driving force of the diffusive dynamics. These chemical potentials can be derived from the thermodynamics of the molecular ensemble. The free energy of the system is in terms of the bead distribution functions, denoted as ψ . The distribution functions of the independent Gaussian chains factorize exactly, and the density functional can be simplified to a product of single-chain density functions. In this

approximation, the free energy functional is written as:

$$F[\psi] = \frac{1}{Q} \int dR (\psi H^{id} + \beta^{-1} \psi \ln \psi) + F^{nid}[\psi].$$

The first term is the average value of the Hamiltonian for the ideal system, comprising the internal Gaussian chain interactions:

$$H^{id} = \sum H_r^G, \text{ where } H_r^G \text{ is the Gaussian chain Hamiltonian of chain: } \beta H_r^G = \frac{3}{2a^2} \sum (R_{r,s} - R_{r,s-1})^2$$

Here a is the Gaussian bond length parameter and the index s goes over all N segments of the chain. The second term in the free energy functional stems from the Gibbs entropy of the distribution. The third term is the non-ideal contribution related to the interchain interactions. In the present mean-field approximation, the latter is independent of the particular distribution ψ .

The constraint minimization of the free energy functional leads to an optimal distribution, which in turn, and by the one-to-one relation between densities, distributions and external potential, can be written:

$$\beta F[\rho] = n \ln \Phi + \beta^{-1} \ln n! - \sum_i \int U_i(r) \rho_i(r) dr + \beta F^{nid}[\rho]$$

Finally, in order to account for the interchain (non-ideal)

interactions, a Flory-Huggins type interaction is introduced:

$$F^{nid}[\rho] = \frac{1}{2} \int \int \varepsilon_{AA}(|r-r'|) \rho_A(r) \rho_A(r') + \varepsilon_{AB}(|r-r'|) \rho_A(r) \rho_B(r') + \varepsilon_{BB}(|r-r'|) \rho_B(r) \rho_B(r') dr dr'$$

where $\varepsilon_{ij}(|r-r'|) \rho_i(r) \rho_j(r')$ is a mean-field energetic interaction between beads of type i at r and type j at r' . This interaction is defined by the same Gaussian kernel as in the ideal chain Hamiltonian: $\varepsilon_{ij}(|r-r'|) = \varepsilon_{ij}^0 \left(\frac{2\pi a^2}{|r-r'|^2} \right) e^{-\frac{3}{2a^2} |r-r'|^2}$.

Donnan electrostatics

The system is closed with respect to changes in the concentrations of the polymer or the solvent, the volume is fixed, but the system is open to changes in ion concentration, coupled to an ion bath. The Helmholtz free energy is:

$$F = F_0 + F_{ion} - \sum_i n_i \mu_i,$$

Where F_0 is the free energy in the absence of electrostatic interactions, F_{ion} is the ion free energy, and μ_i is the chemical potential of ion type i . F has to be minimized with the electroneutrality constraint in place, for which an additional Lagrange multiplier field, λ , the so-called Donnan potential is

introduced, and minimize:

$$F' = F + kT \int \lambda Q dr,$$

where Q is the net charge at position r , defined as $Q = Q_p + \sum z_i \rho_i$, where $Q_p = \sum_i z_i \rho_i$ is the net polymer charge (polymers are denoted with capitalized subscripts) the sum is over the electrolyte ions and ρ_i is the number concentration of ions.

The mean field free energy for the ion interactions is:

$$F_{ion} = kT \sum_i \int_V \rho_i [\ln \lambda^3 \rho_i - 1] dr + kT \sum_{ij} \int_V a_{ij} \rho_i \theta_j dr$$

Where λ is the thermal wavelength, a_{ij} is an ion-polymer interaction parameter, and

$\theta_j = v \rho_j$ is the volume fraction of polymer j .

The ion exchange potential, μ_i , are calculated in the external bath, and since the bath is neutral: $\mu_+ = \mu_- = \mu_s$.

$$\sum_i \mu_i n_i = \mu_s \int \sum_i \rho_i dr.$$

In the dynamical phase separation process, it is assumed that:

(1) Ions diffuse so fast that they are in constant internal equilibrium. (2) The net charge at each point in space is zero. (3) The chemical potential of the external bath is constant.

These three conditions correspond to two equations for the free energy derivatives:

$$\frac{\delta F}{\delta \rho_i} = 0 = kT \ln \lambda^3 \rho_i + kT \sum_i a_{il} \theta_l - \mu_s + kT \lambda z_i,$$

and one equation for the reference chemical potential, which is assumed to be ideal:

$$\mu_s = kT \ln \lambda^3 c_s.$$

The third condition above can be changed; in this way, the total number of ions can be fixed. With the assumption of fixed chemical potentials, the number of ions may vary depending on the morphology. When the system contains more salt than the total polymer charge, the difference between closed and open systems vanishes.

The intrinsic chemical potential of the polymer is:

$$\frac{\delta F}{\delta \rho_i} = \mu_i^0 + \mu_i^D \text{ and } \frac{\mu_i^D}{kT} = \sum_i a_{il} v \rho_l + \lambda z_i,$$

where μ_i^D is the contribution of the Donnan equilibrium to the intrinsic chemical potential. The case where the interactions with the polymer matrix are not specific is simplified by $a_{+l} = a_{-l} = a_l$. The partition coefficient is defined as

$$K = e^{\sum_i \mu_i \theta_i} = \prod_i (K_i^0)^{\theta_i}.$$

The partition function for the pure polymers is K_l^0 . The ion equilibrium gives:

$$\rho_i = c_s K \exp[-z_i \lambda].$$

Combination with the electroneutrality condition gives:

$$Q_p = 2c_s K \sinh \lambda, \quad \lambda = \sinh^{-1} \left[\frac{Q_p}{2Kc_s} \right].$$

Returning to the expression for the free energy and using the third condition:

$$F = F^0 + \int \lambda Q_p dr - kT \sum_i \int_V \rho_i dr,$$

Which can be rewritten in the convenient form:

$$F = F^0 + 2kT \int_V c_s K [\lambda \sinh \lambda - \cosh \lambda] dr$$

Notes and references

^a Advanced Photonics Center, School of Electronic Science and Engineering, Southeast University, Nanjing, 210096, China. E-mail: cyp@seu.edu.cn

^b Institute of Research on the Structure and Property of Matter, Zaozhuang University, Shandong 277160, China. E-mail: mudanjlu1980@163.com

^c School of Chemistry and Chemical Engineering, Shandong University,

- Jinan 250100, Shandong, China; E-mail: fsy@sdu.edu.cn
- 1 S.O. Kim, H.H. Solak, M.P. Stoykovich, N.J. Ferrier, J.J. de Pablo and P.F. Nealey, *Nature*, 2003, **424**, 411.
 - 2 A. Rösler, G.W.M. Vandermeulen and H.A. Klok, *Adv. Drug Deliver. Rev.*, 2012, **64**, 270.
 - 3 P. Bhargava, Y.F. Tu, J.X. Zheng, H.M. Xiong, R.P. Quirk and S.Z.D. Cheng, *J. Am. Chem. Soc.*, 2007, **129**, 1113.
 - 4 F.E. Bailey and J.V. Koleske, *Poly(ethylene oxide)*, New York: Academic Press, 1976, p. 163.
 - 5 S. Patel, R.S. Thakar, J. Wong, S.D. Mcleod and S. Li, *Biomaterials*, 2006, **24**, 2890.
 - 6 H. Chiu, C.S. Chern, C.K. Lee and H.F. Chang, *Polymer*, 1998, **39**, 1609.
 - 7 S.R. Guo, L.J. Shen and L.X. Feng, *Polymer*, 2001, **42**, 1017-1022.
 - 8 T. Eisa and M.V. Selfton, *Biomaterials*, 1993, **14**, 755.
 - 9 D.J. Siegwart, W. Wu, T. Kowalewski, J.O. Hollinger and K. Matyjaszewski, *Polym. Prepr.*, 2005, **46**, 399.
 - 10 D. Mu, X.R. Huang, Z.Y. Lu and C. C. Sun, *Chem. Phys.*, 2008, **348**, 122.
 - 11 H. Ito, T.P. Russell and G.D. Wignall, *Macromolecules*, 1987, **20**, 2213.
 - 12 A.C. Fernandes, J.W. Barlow and D.R. Paul, *J. Appl. Polym. Sci.*, 1986, **32(6)**, 5481.
 - 13 I. Hopkinson, F.T. Kiff and R.W. Richards, *Polymer*, 1995, **18**, 3523.
 - 14 J.G.E.M. Fraaije, B.A.C. van Vlimmeren, N.M. Maurits, M. Postma, O.A. Evers, C. Hoffmann, P. Altevogt and G. Goldbeck-Wood, *J. Chem. Phys.*, 1997, **106**, 4260.
 - 15 B.A.C. van Vlimmeren, N.M. Maurits, A.V. Zvelindovsky, G.J.A. Sevink and J.G.E.M. Fraaije, *Macromolecules*, 1999, **32**, 646.
 - 16 Y.M. Lam and G. Goldbeck-Wood, *Polymer*, 2003, **44**, 3593.
 - 17 N.M. Maurits, G.J.A. Sevink, A.V. Zvelindovsky and J.G.E.M. Fraaije, *Macromolecules*, 1999, **32**, 7674.
 - 18 Y.M. Li, G.Y. Xu, D. Wu and W.P. Sui, *Eur. Polym. J.*, 2007, **43**, 2690.
 - 19 S.L. Guo, T.J. Hou and X.J. Xu, *J. Phys. Chem. B*, 2002, **106**, 11397.
 - 20 D. Mu, J.Q. Li and S. Wang, *J. Appl. Polym. Sci.*, 2013, **127(3)**, 1561.
 - 21 D. Mu, J.Q. Li and S.Y. Feng, *Polym. Int.*, 2014, **63(3)**, 568.
 - 22 D. Mu, J.Q. Li and S. Wang, *J. Appl. Polym. Sci.*, 2011, **122(1)**, 64.
 - 23 D. Mu, J.Q. Li and S. Wang, *J. Polym. Res.*, 2012, **19(7)**, 9910.
 - 24 D.D. Wang, Z.P. Peng, X.X. Liu, Z. Tong, C.Y. Wang and B.Y. Ren, *Eur. Polym. J.*, 2007, **43**, 2799.
 - 25 H. Desai, D. Varade, V.K. Aswal, P.S. Goyal and P. Bahadur, *Eur. Polym. J.*, 2006, **42**, 593.
 - 26 G.J. Zhao, J.Y. Liu, L.C. Zhou and K.L. Han, *J. Phys. Chem. B*, 2007, **111**, 8940.
 - 27 G.J. Zhao and K.L. Han, *Accounts Chem. Res.*, 2012, **45(3)**, 404.
 - 28 O. Altintas, A.P. Vogt, C. Barner-Kowollik, and U. Tunca, *Polym. Chem.*, 2012, **3**, 34.
 - 29 G. Ungar, C. Tschierske, V. Abetz, R. Holyst, M.A. Bates, F. Liu, M. Prehm, R. Kieffer, X. Zeng, M. Walker, B. Glettner and A. Zywockinski, *Adv. Funct. Mater.*, 2011, **21**, 1296.
 - 30 T. Higashihara, M. Hayashi and A. Hirao, *Prog. Polym. Sci.*, 2011, **36**, 323.
 - 31 S. Ito, R. Goseki, T. Ishizone and A. Hirao, *Eur. Polym. J.*, 2013, **49**, 2545.
 - 32 S. Ito, R. Goseki, T. Ishizone, S. Senda and A. Hirao, *Macromolecules*, 2013, **46**, 819.
 - 33 S. Junnila, N. Houbenov, A. Karatzas, N. Hadjichristidis, A. Hirao, H. Iatrou and O. Ikkala, *Macromolecules*, 2012, **45**, 2850.
 - 34 J.G. Ray, A.J. Johnson, D.A. Savin, *J. Polym. Sci. Part B: Polym. Phys.*, 2013, **51**, 508.
 - 35 T. Satoh, N. Nishikawa, D. Kawato, D. Suemasa, S. Jung, Y.Y. Kim, M. Ree and T. Kakuchi, *Polym. Chem.*, 2014, **5**, 588.
 - 36 R. Jahn and H. Grubmuller, *Curr. Opin. Cell Biol.*, 2002, **14**, 488.
 - 37 J. Fraaije, B. Van Vlimmeren, N. Maurits, M. Postma, O. Evers, C. Hoffmann, P. Altevogt and G. Goldbeck-Wood, *J. Chem. Phys.*, 1997, **106**, 4260.
 - 38 P. Altevogt, O.A. Evers, J.G.E.M. Fraaije, N.M. Maurits and B.A.C. van Vlimmeren, *J. Mol. Struct-Theochem.*, 1999, **463**, 139.
 - 39 S.S. Jawalkar and T.M. Aminabhavi, *Polymer*, 2006, **47(23)**, 8061.
 - 40 A.F.M. Barton, *Handbook of Solubility Parameters and Other Cohesion Parameters*, CRC Press, Boca Raton, FL, 1993.
 - 41 A. Choucair and A. Eisenberg, *J. Am. Chem. Soc.*, 2003, **125**, 11993.
 - 42 L. Xing and W.L. Mattice, *Macromolecules*, 1997, **30**, 1711.
 - 43 Accelrys Software, Inc., 2007, *Materials Studio online help: MesoDyn*. Accelrys Software, Inc., San Diego.